

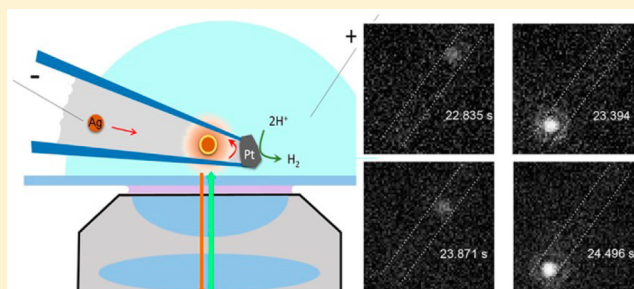
Imaging Dynamic Collision and Oxidation of Single Silver Nanoparticles at the Electrode/Solution Interface

Rui Hao,[†] Yunshan Fan,[†] and Bo Zhang*[✉]

Department of Chemistry, University of Washington, Seattle, Washington 98195, United States

S Supporting Information

ABSTRACT: The electrochemical interface is an ultrathin interfacial region between the electrode surface and the electrolyte solution and is often characterized by numerous dynamic processes, such as solvation and desolvation, heterogeneous electron transfer, molecular adsorption and desorption, diffusion, and surface rearrangement. Many of these processes are driven and modulated by the presence of a large interfacial potential gradient. The study and better understanding of the electrochemical interface is important for designing better electrochemical systems where their applications may include batteries, fuel cells, electrocatalytic water splitting, corrosion protection, and electroplating. This, however, has proved to be a challenging analytical task due to the ultracompact and dynamic evolving nature of the electrochemical interface. Here, we describe the use of an electrochemical nanocell to image the dynamic collision and oxidation process of single silver nanoparticles at the surface of a platinum nanoelectrode. A nanocell is prepared by depositing a platinum nanoparticle at the tip of a quartz nanopipette forming a bipolar nanoelectrode. The compact size of the nanocell confines the motion of the silver nanoparticle in a 1-D space. The highly dynamic process of nanoparticle collision and oxidation is imaged by single-particle fluorescence microscopy. Our results demonstrate that silver nanoparticle collision and oxidation is highly dynamic and likely controlled by a strong electrostatic effect at the electrode/solution interface. We believe that the use of a platinum nanocell and single molecule/nanoparticle fluorescence microscopy can be extended to other systems to yield highly dynamic information about the electrochemical interface.



INTRODUCTION

The past decade has seen an enormous growth in studying individual nanoparticles (e.g., metal, semiconductor, and insulating polymer) in electrochemistry and electrocatalysis.^{1–5}

This field of research is driven primarily by a strong interest in the use of nanoparticles as a key catalytic material for various technological applications such as fuel cells,^{6–9} catalytic water splitting,^{10–12} and photovoltaics.^{13–16} Compared to traditional ensemble methods, the ability to probe electrocatalytic property of single nanoparticles enables one to remove ensemble averaging in understanding their structure–function relationship.² Another advantage of studying single-nanoparticle electrochemistry is the easily detectable transient redox signal associated with one particle interacting with the electrode surface thanks to their larger size and tunable electrochemical activity.

Some of the pioneering reports include Lemay's study of nanoparticle adsorption on a gold ultramicroelectrode¹⁷ and Bard's work on nanoparticle collision and electrocatalytic amplification.^{18,19} Despite the fact that both of these methods detect transient nanoparticle collision events, they are based on two distinct mechanisms. Lemay's work used large polymer beads which lead to current suppression due to particles blocking the diffusion of redox molecules to the electrode surface. On the other hand, Bard's group studied small metal

(e.g., Pt and Au) nanoparticles which catalyze the oxidation or reduction of an inner-sphere redox species resulting in discrete current increase. Both methods have received considerable attention and have been extended to the study of many other species. Another useful method is based on the oxidation or reduction of the nanoparticle itself during a collision event.²⁰ Metal nanoparticles, such as gold²¹ and silver,²² can be easily oxidized on an electrode leading to a detectable faradaic signal. We and two other groups have reported the observation of the multiplex collision behavior of single silver nanoparticles.^{23–25}

As a necessary tool in single nanoparticle studies, microelectrodes allow one to reduce and control both the collision frequency and the electrical noise which often scale with the total area of the electrode.²⁶ Although most of the previous studies have used carbon^{27–29} or metals^{30–33} ultramicroelectrodes, the use of nanoelectrodes^{34–37} and carbon nanopipettes³⁸ has enabled direct recording of discrete adsorption events of individual small molecules and electrocatalytic collision events of isolated metal nanoparticles, respectively. On the other hand, the use of liquid metals³⁹ and chemically functionalized³³ ultramicroelectrodes have opened new opportunities in highly sensitive detection, understanding nanoparticle deactivation,

Received: June 20, 2017

Published: August 11, 2017

and studying specific biological interactions. Combining with the ability to optically observe single nanoparticles,^{3,40,41} one can possibly develop a more detailed understanding of the dynamic redox behavior at the electrode/solution interface. Toward this goal, Tao's group used plasmonic imaging technique to study collision and electrochemical oxidation of single Ag nanoparticles.⁴² Crooks' group reported correlated electrochemical and optical tracking of discrete collision of fluorescent beads on a microelectrode.⁴³ Tessier and Kanoufi used holographic microscopy to study collision of silver nanoparticles providing unique information in the Z direction from reconstructed 2D images.^{44–46} The Kanoufi group also studied the silver nanoparticle collisions by coupled dark field microscopy and spectroscopy.⁴⁷

Despite the significant progress in collision-based single-nanoparticle electrochemistry, detailed understanding of the dynamic behavior of individual nanoparticles at the electrode/solution interface has been quite limited. There are several reasons leading to this fact. First, most of the previous studies have used current measurements under either constant or sweeping potentials. Second, the small dimension of the nanoparticle itself and its fast diffusional motion at the electrode/solution interface make it very challenging if not impossible for optical-based imaging with sufficient spatial and temporal resolutions. Third, the nanoscale interfacial area at the electrode/solution interface is likely beyond the optical resolution of most microscopy methods when the electrode is imaged in the transmission, reflection or scattering mode.

Identifying this limitation, we have designed and used a unique nanoscale electrochemical cell to image and capture the dynamic collision and oxidation behavior of single silver nanoparticles at the electrode/solution interface. Figure 1 is a

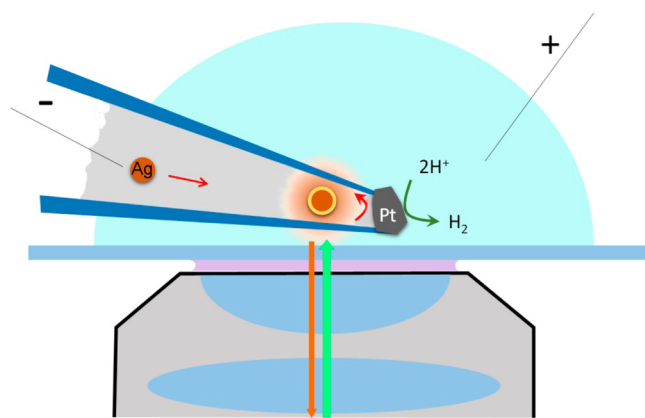


Figure 1. A cartoon of the experimental setup used to image single nanoparticle collision in a nanopipette electrochemical cell. A Ag nanoparticle collides on the Pt nanoelectrode surface and is partially oxidized resulting in the formation of Ag_2O . The oxide layer is photodecomposed leading to the formation of small silver clusters, which generates strong fluorescence signal. The oxidation of silver inside the nanocell is electrically coupled to the reduction of protons on the external surface of the Pt.

cartoon illustrating the experimental setup used to image single nanoparticles in a nanopipette electrochemical cell. A unique Pt nanoelectrode is constructed inside a quartz nanopipette which confines the motion of the silver nanoparticle in a volume down to ~ 50 attoliters. Placing the tip of the quartz nanopipette horizontally on an inverted microscope allows us to optically image the interfacial region on the Pt nanoelectrode surface.

The oxidation of the silver nanoparticle inside the nanopipette is electrically coupled to the reduction of protons on the external surface of the Pt with a bipolar electrochemistry mechanism. Fluorescence imaging of individual silver nanoparticles prior to and after collision on the Pt nanoelectrode are based on their residual surface oxide and the oxidative formation of silver oxide, respectively. We used the technique of super-resolution localization⁴⁸ to resolve transient changes in the nanoparticle position relative to the electrode surface with a < 50 nm spatial resolution and < 10 ms temporal resolution. With this method, we have demonstrated the unique ability to optically resolve dynamic motion of individual nanoparticles during their collision and oxidation at the electrode/solution interface. We have discovered that the collision and oxidation lead to a transient increase in nanoparticle fluorescence. The fluorescence decays as the particle momentarily diffuses away from the electrode indicating dissolution and decomposition of surface oxide. Multiple collisions are typically observed on each particle along with micrometer-long diffusional paths before complete particle dissolution or particle escaping from the interfacial region. We believe the dynamic collision behavior is controlled by strong electrostatic interactions between the nanoparticle and the charged surfaces of the electrode and the quartz walls. This method opens up new opportunities in the study of dynamic behavior of single nanoparticles and molecules at the electrochemical interface.

■ EXPERIMENTAL SECTION

Chemicals and Materials. All the following chemicals and materials were used as received from the manufacturers. Acetonitrile (ACN, Fisher Scientific, 99.9%), ferrocene (Fc, Fluka, 98.0%), lithium perchlorate (LiClO_4 , Aldrich, 99.99%), sodium citrate dihydrate (J. T. Baker, 100.1%), sodium nitrate (NaNO_3 , Sigma-Aldrich, 99.0%), perchloric acid (HClO_4 , Sigma-Aldrich, 70%), 40 nm diameter silver NPs (sodium citrate capped, dispersed in 2 mM citrate, Nano-Composix, Inc. San Diego, CA). All aqueous solutions were prepared using deionized water (> 18 M Ω cm) from a Barnstead Nanopure water purification system.

Preparation of Pt Nanocells. Quartz nanopipettes were prepared by pulling quartz capillary (0.5 mm I.D./1.0 mm O.D., with filament) by a P-2000 laser puller with the following pulling program: heat = 650, filament = 4, velocity = 90, delay = 140, pull = 200. FIB milling/deposition and SEM imaging were performed on an FEI XL830 Dual Beam system, in which there is an angle of 52° between the e-beam and ion beam. The nanopipettes were mounted horizontally on the stage. Without tilting the stage, the angle between the ion beam (from the source to the substrate) and the nanopipettes (from the bottom to the sharp tip) was 52° . The tips of nanopipettes were milled with line scan ($L = 1 \mu\text{m}$, $d = 1 \mu\text{m}$) at the position of certain diameter (200 nm for E100, 600 nm for E300) with the current of 4 pA or 11 pA in Insulator Enhanced Etching (IEE) mode. Nanocells with larger electrode size can be prepared with a similar approach with increased milling ion current. The stage was then rotated 180° for Pt deposition. Area scans ($d = 500$ nm) of 400×500 nm at 1 pA (E100) or 500×600 nm at 4 pA (E300) were used on the orifice of the milled nanopipette in Pt deposition mode. Afterward, the nanocells were ready to use.

Fabrication of Ag Disk Microelectrode. The 100- μm diameter Ag disk microelectrode was fabricated by sealing a 100 μm diameter Ag microwire (Alfa-Aesar) in a piece of borosilicate capillary (Sutter Instrument Co.) and making connection to the Ag with tungsten wire and Ag paint (DuPont) through the back end of the capillary.

Fluorescence Imaging of Single Ag/ Ag_2O Nanoparticles. A Pt nanocell containing 95 pM 40 nm Ag NPs and 2 mM citrate was immersed in a drop of 0.1 M HClO_4 solution and placed horizontally (angle between the nanocell and coverslip was about 10°) on a coverslip on an Olympus IX70 inverted microscope for observation.

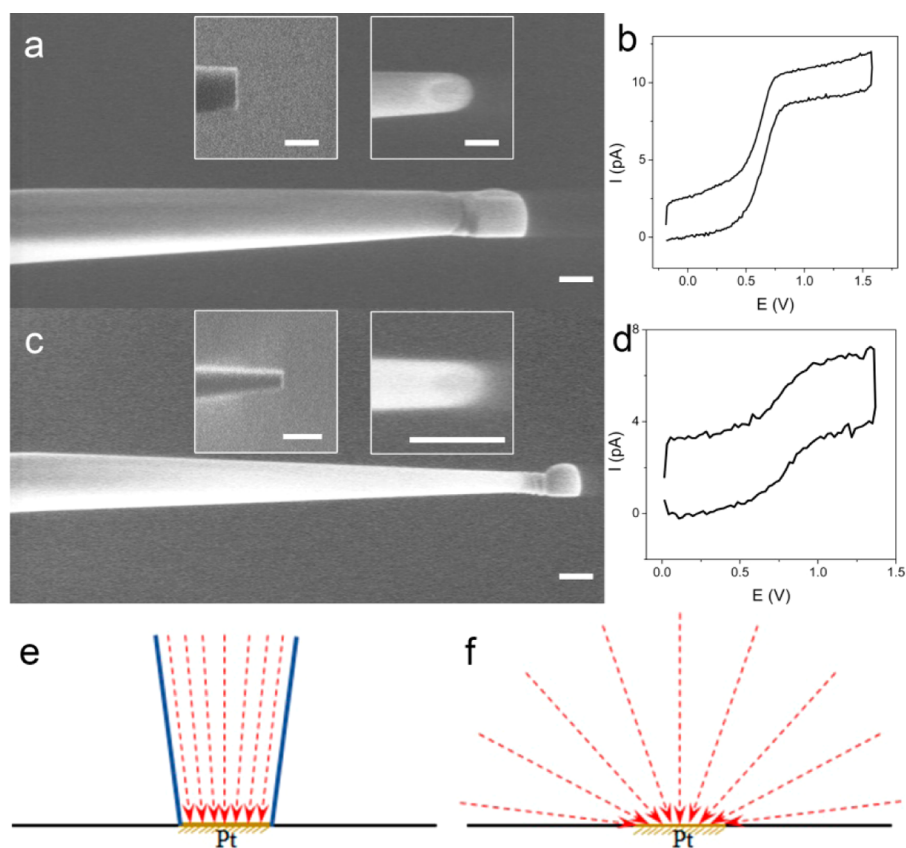


Figure 2. (a,c) SEM images of two Pt nanocells with inner electrode diameters of about 300 nm (a) and 100 nm (c). The insert images were milled quartz nanopipettes before Pt deposition (Left: 52° ion-beam images, right: top-view e-beam images). All scale bars represent 500 nm. (b,d) Corresponding cyclic voltammograms at 100 mV/s of the Pt nanocells shown in (a,c) filled with acetonitrile containing 5 mM ferrocene and 0.2 M LiClO_4 . The nanocells were immersed in 100 mM perchloric acid. (e,f) A comparison of the diffusion profiles inside a Pt nanocell vs on a Pt nanodisk electrode.

The excitation source was a solid-state 532 nm green laser (CrystaLaser) emitting at 40 mW configured for epifluorescence. The fluorescence signal was collected by a $100\times$ 1.30 NA objective (Olympus UPlanFL) and optically filtered using an ET610/75m emission filter (Chroma Technology). An additional $1.5\times$ magnification on the microscope was used. An Andor iXon EMCCD camera cooled to -85°C and Andor SOLIS software were used to record all images. Images were recorded by using an exposure time of either 5 ms (frame rate: 182.48 Hz) or 20 ms (frame rate: 48.828 Hz), as indicated in the article. An amplifier gain of 300 as well as a preamplifier gain of 5.1 were used. The voltage function was generated by a potentiostat (Princeton Applied Research Model 273A) and applied across the two driving electrodes (a Ag QRE inside the nanocell and a Pt QRE outside of the nanocell).

Fluorescence Imaging of 100- μm Ag Microelectrode. A 100- μm Ag microelectrode was immersed in a 2 mM citrate solution and placed vertically above a coverslip on an Olympus IX70 inverted microscope for observation. The excitation source was a solid-state 532 nm green laser (CrystaLaser) emitting at 40 mW configured for epifluorescence. The fluorescence signal was collected by a $4\times$ 0.13 NA objective (Olympus UPlanFL) and optically filtered using an ET610/75m emission filter (Chroma Technology). An Andor iXon EMCCD camera cooled to -85°C and Andor SOLIS software were used to record all images. Images were recorded by using an exposure time of 20 ms, giving a frame rate of 48.828 Hz. A preamplifier gain of 5.1 was used. The voltage function was generated by a potentiostat (Princeton Applied Research Model 273A) and applied on the Ag microelectrode with respect to a Pt QRE.

Image Analysis. Single-nanoparticle fluorescence images were analyzed using ThunderSTORM plug-in in ImageJ.⁴⁸ Each fluorescent single nanoparticle spot is described by a point spread function (PSF),

which is fitted with a two-dimensional (2-D) Gaussian function using maximum-likelihood estimation to achieve subdiffraction localization of single nanoparticles. The photon counts of each fluorescent burst on one frame were converted from the total integrated fluorescence signal counts under the fitted 2-D Gaussian function using ThunderSTORM.

Electrochemical Measurements. The single-particle amperometry experiments were carried out using a potentiostat (Princeton EG&G PARC Model 175 Universal Programmer) integrated with a low noise current amplifier (Electro Optical Components, Inc. model: LCA-1K-5G) interfaced to a PC through a Digidata 1322A digitizer (Axon Instruments, Inc.). Amperometric traces were recorded using pClamp 10.4 Axoscope software (Molecular Devices) with a 100 kHz sampling rate. Current spikes were analyzed and integrated using pClamp 10.4 Clampfit software (Molecular Devices).

RESULTS AND DISCUSSION

Preparation and Characterization of the Pt Nanocell.

A key to the successful imaging of nanoparticle collision is the development and use of the Pt nanocell. The bipolar nanocell is prepared by depositing a Pt nanoparticle at the tip of a laser-pulled quartz nanopipette. The inner and outer surfaces of the Pt nanoparticle are immersed in two separate compartments. A pair of metal wire electrodes is used to supply a voltage across the Pt driving two separate redox reactions on the opposite Pt surfaces. As described in the [Experimental Section](#), Pt nanocells with inside diameters between 50 to 1000 nm can be reproducibly fabricated using focused-ion beam (FIB)-assisted deposition of Pt at the pipet pore.

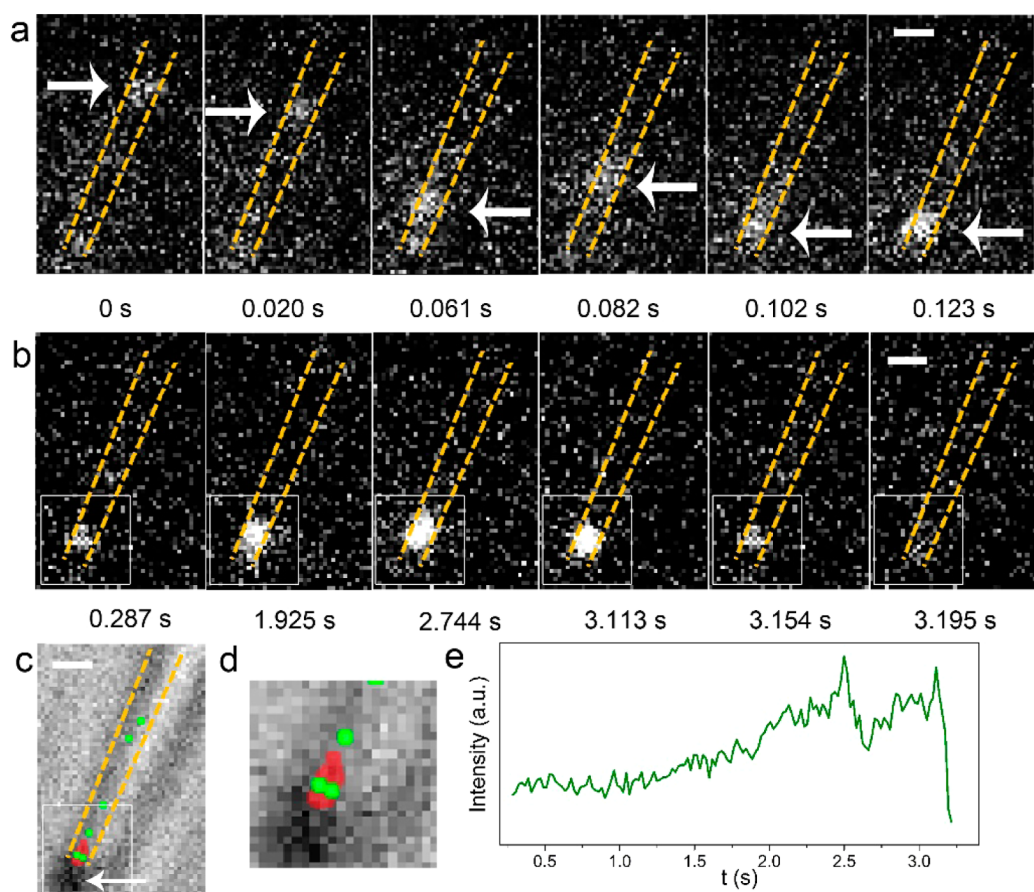


Figure 3. Visualizing nanoparticle collision and oxidation inside an E300 Pt nanocell. (a) A single silver nanoparticle, which is indicated by the white arrows, moving along the E300 nanocell toward the Pt electrode under +1.5 V applied voltage. (b) Fluorescence images of the same nanoparticle at different time points while interacting with the Pt electrode. (c) Overlaid images of the super-resolution mapping of the nanoparticle and the bright-field image of the E300 nanocell, in which green dots indicate the location of the NPs from $t = 0$ s to $t = 0.123$ s and the red dots indicate the location of the NPs afterward. The large solid dot in the bright-field image, which is indicated by the white arrow, is considered as the Pt electrode. (d) Magnified overlaid images of marked square-shaped area in (c). (e) The intensity profile of the marked square-shaped area in (b). The fluorescent images were recorded with a frame rate of 48.828 Hz and an exposure time of 20 ms. The scale bars represent 1 μm .

Figure 2a and 2c display SEM images of two Pt nanocells having inside diameters of 300 and 100 nm, respectively. The insets are SEM images taken at two different angles of the same quartz nanopipettes prior to Pt deposition. The effective electrode area inside a Pt nanocell is thus defined by the inner diameter of the quartz at the tip. The small size of the inner Pt surface and the long and restricted pipet volume limit the diffusion rate of redox species. This in turn limits the diffusion-limited electrochemical current signal one can achieve on such Pt bipolar nanocells. The external Pt surface area can be intentionally made much greater than that of the inner Pt. Considering the greater open space in the external solution, the larger Pt size, and the higher redox concentration, the overall faradaic response is likely limited by the redox reactions⁴⁹ inside the nanocell volume. This allows one to focus the discussion on the redox reaction on the inner Pt surface.

Pt nanocells with inner diameters of about 300 nm, denoted as E300, and 100 nm, denoted as E100, were primarily used in this study. Cyclic voltammetry was first used to characterize their electrochemical responses. Here, oxidation of ferrocene on the inner Pt surface is coupled to the reduction of protons on the external Pt surface. The coupled reactions were driven by a Pt wire placed in the external solution and a piece of Ag wire from inside the pipet. Figure 2b and 2d show the cyclic

voltammograms at 100 mV/s of the E300 and E100 nanocells each containing 5 mM ferrocene and 200 mM LiClO₄ in acetonitrile. The external Pt is immersed in 100 mM perchloric acid. Both electrodes show sigmoidal shape CVs indicating diffusion-limited steady-state electrochemical behavior. The onset potentials for ferrocene oxidation are about 0.5 V and the steady-state limiting currents are about 9 pA and 3 pA for E300 and E100, respectively. Considering that the standard electrode potential of ferrocene is +0.64 V vs normal hydrogen electrode (NHE), the minor potential shift is likely due to the added ion-transfer resistance in the nanopipette and the use of two different driving electrode wires. The small limiting currents (3 pA and 9 pA for the 100 and 300 nm nanocells, respectively) relative to disk-shaped Pt nanoelectrodes of similar sizes can be qualitatively understood by the restricted diffusion rates of ferrocene inside a nanopipette. Figure 2e and 2f display a comparison of the diffusion profiles of a Pt nanocell and a Pt disk nanoelectrode. The predicted limiting currents are about 250 and 750 pA on a 100 and 300 nm disk nanoelectrodes,⁵⁰ respectively, when placed in 5 mM ferrocene, which are nearly 2 orders of magnitude greater than that measured on the nanocells.

Fluorescence Imaging of Nanoparticle Collision. To directly visualize single nanoparticle collision, we set up an

experiment by filling an E300 nanocell with a 2 mM citrate buffer (pH 7.9) containing 95 pM nominal 40 nm Ag nanoparticles and immersing the Pt tip inside 100 mM perchloric acid. The nanocell was illuminated with a 40 mW 532 nm green laser and the fluorescence images and videos were collected at 610 ± 37.5 nm. A voltage of +1.5 V was applied across the Pt particle to drive the oxidation of Ag nanoparticles inside the nanocell. The nearly horizontal placement of a Pt nanocell and the use of fluorescence enable us to directly capture the fast motion of single Ag nanoparticles during their collision and oxidation on the surface of the Pt nanoelectrode. An example video showing the dynamic collision behavior of a 40 nm Ag nanoparticle in an E300 Pt nanocell is given in the Supporting Information as Video S1. Figure 3a includes a series of six fluorescence images collected in this video showing the nanoparticle approaching the Pt surface inside the nanocell under a +1.5 V driving potential. During the initial 0.061 s, the particle is seen to approach the Pt tip along the direction of the nanochannel. At 0.082 s (the fourth image of Figure 3a), the nanoparticle appears further away from the Pt than at 0.061 s and 0.102 s. The overall approaching trajectory and the slight motion in the reverse direction suggest that the overall particle motion in this initial stage is controlled by electrostatic attraction between the negatively charged nanoparticle and the positive Pt surface. However, the particle is also affected by Brownian motion and the electrostatic repulsion from the negatively charged quartz walls.

Interestingly, starting at 0.123 s, the Ag nanoparticle is only seen within the close vicinity of the Pt nanoelectrode, as shown in Figure 3b. Here, we used the technique of super-resolution mapping⁴⁸ to further determine the location of the Ag nanoparticle at each time point (see Image Analysis in the Experimental Section for the procedure of particle localization). By plotting and overlaying these locations (Figure 3c,d), one can clearly see the two separate stages the nanoparticle undergoes near the electrode surface. The green dots indicate particle locations in the first 0.123 s while the red dots represent nanoparticle locations collected after its initial contact with the electrode. Most of the red dots are located within a ~ 500 nm distance from the Pt electrode. The close proximity of nanoparticle suggests that the particle motion is strongly controlled by electrostatic interaction between the electrode and the surface of the Ag nanoparticle. This is an exciting result because it clearly reveals that there is complex and dynamic particle motion involved during particle collision and dissolution at the electrode/solution interface.

One of the most remarkable results obtained in this work is the observation of the dynamic fluctuation of the fluorescence intensity of the Ag nanoparticle during its collision and oxidation on the Pt nanoelectrode. We can see from Figure 3b that the intensity of the Ag nanoparticle changes when it interacts with the electrode. This is in stark contrast to the nearly constant particle intensity prior to particle contacting the electrode. Figure 3e displays a fluorescence intensity profile of the marked nanoelectrode area as shown in Figure 3b. The fluorescence intensity of the nanoparticle increased gradually with time and then after a drastic decrease, no more obvious nanoparticle fluorescence signal can be detected. Similar phenomenon can be reproducibly observed on other nanoparticles and in other Pt nanocells. Another example is given in Figure S2, which shows scattered nanoparticle locations of another 40 nm Ag nanoparticle inside an E300 Pt nanocell

during its collision and interaction on the Pt electrode. The range of particle motion is found to be restricted within about 1 μm along the nanocell (vertical to the electrode surface), which is about 5 times greater than the range of motion in other dimensions. The fluorescence intensity of the nanoparticle (Figure S2d) is also found to increase gradually and decrease rapidly to the background.

We believe the quick increase and decrease in nanoparticle fluorescence are caused by particle oxidation and formation of Ag_2O on nanoparticle surface and its subsequent photo-reduction and dissolution. Ag_2O itself is not significantly fluorescent. However, under intensive light illumination, Ag_2O can undergo photoreduction and photodissociation generating small Ag clusters which are strongly fluorescent.^{51,52} As such, it is reasonable to believe that the transient increase in fluorescence intensity is caused by collision-induced particle oxidation and the formation of Ag_2O on the particle surface.

To further confirm this hypothesis, we measured the fluorescence response of a 100 μm diameter disk Ag microelectrode during its electro-oxidation in a 2 mM sodium citrate solution. The same green laser was used to illuminate the electrode surface and fluorescence was collected using the same emission filter. The fluorescence was collected as a function of the electrode potential when the potential was scanned linearly from -1 to 1 V vs a Pt QRE at a scan rate of 100 mV/s. Figure 4a is the fluorescence CV collected on this electrode. An apparent fluorescence increase can be observed at an onset potential of around +0.3 V. The fluorescence intensity keeps increasing until 1 V and then decreases back to the

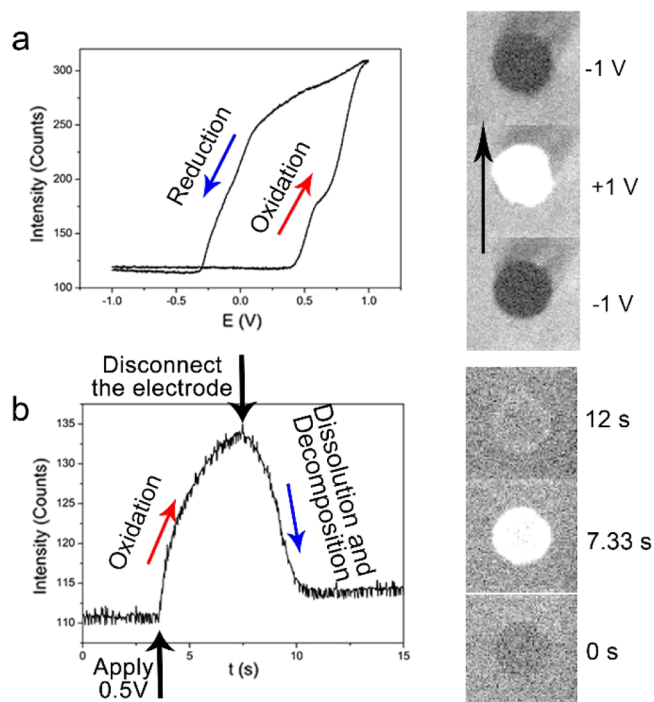


Figure 4. (a) A fluorescence-potential plot of a 100 μm diameter disk Ag electrode collected at 100 mV/s scan rate and the corresponding fluorescence images of the electrode taken at two different potentials (-1 V initial, +1 V, and -1 V final). (b) A fluorescence-time plot of the same Ag electrode showing the formation of silver oxide with applied potential (+0.5 V) followed by a quick decrease after breaking the circuit. The right panel shows fluorescence images of the same electrode taken at three different time points.

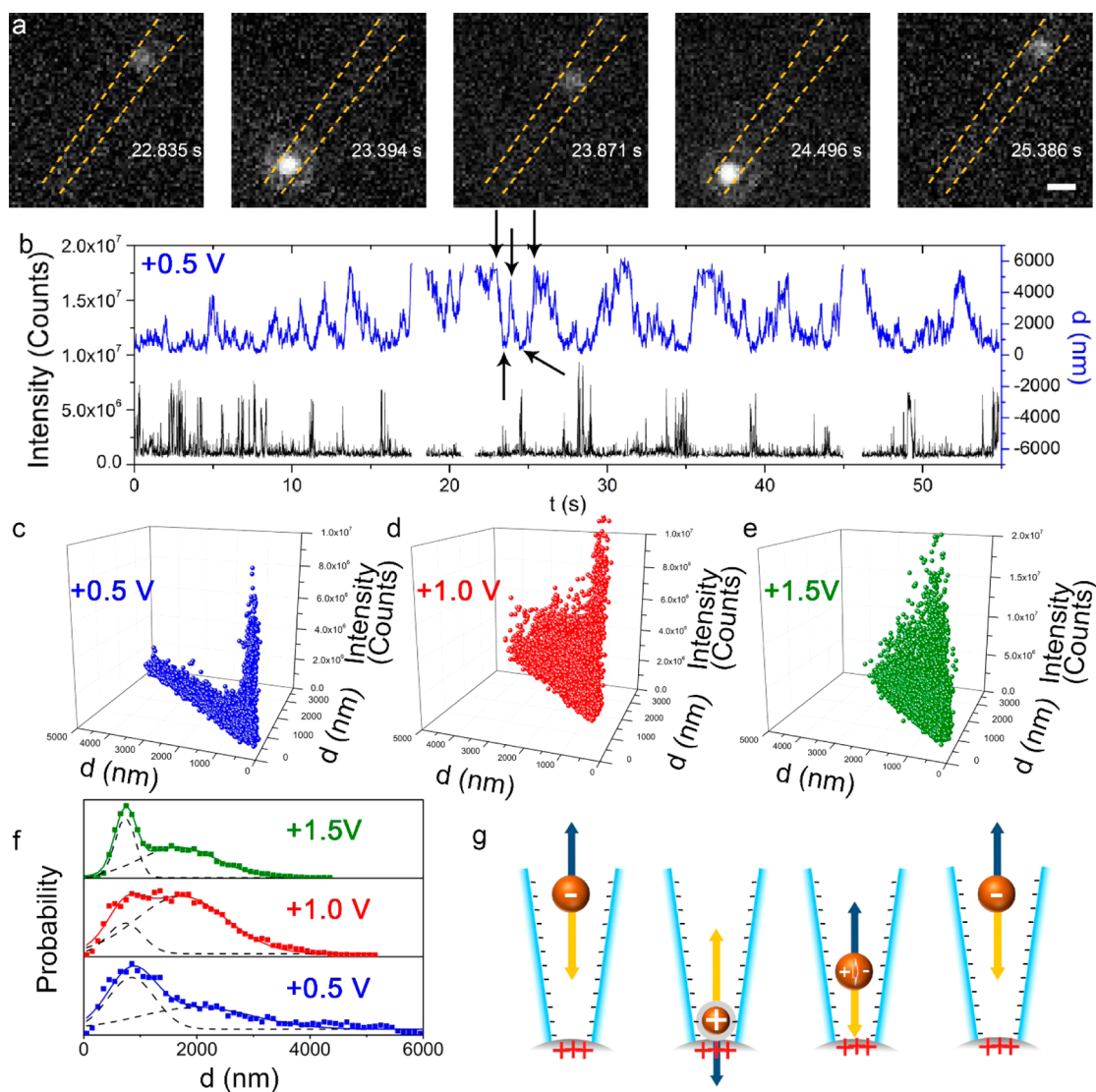


Figure 5. Imaging nanoparticle collision in an E100 Pt nanocell. (a) Fluorescent images of a single silver nanoparticle inside an E100 nanocell. Scale bar represents 1 μm . (b) The fluorescence intensity (black) of the silver nanoparticle and its distance (blue) to the Pt electrode plotted vs time. The arrows indicate the time points at which the fluorescence images are taken in (a). (c–e) 3D scatter plots at three different voltages (+0.5 V, +1.0 V, and +1.5 V) of the fluorescence intensity of the nanoparticle vs its relative position on the focal plane. (f) The probability of finding the nanoparticle vs the particle–electrode distance at three different potentials. (g) A cartoon illustrating different electrostatic forces the silver nanoparticle experiences at four different stages: (1) prior to particle collision with the Pt, the silver nanoparticle experiences both electrostatic repulsive force from the negatively charged quartz wall and the attractive force from the positive Pt surface; (2) during a collision event, the surface of the nanoparticle is in electrical contact with the Pt resulting in positive charges on the silver. The positively charged nanoparticle is now repelled by and moves away from the electrode; (3) dissolution of silver oxide and readorption of citrate ligands on the silver particle surface lead to negatively charged particle; and (4) the nanoparticle is attracted toward the Pt electrode when sufficient negative charges are accumulated on its surface. The fluorescent images were recorded with a frame rate of 182.48 Hz and an exposure time of 5 ms.

baseline when the potential is scanned in the reverse direction. This result supports our hypothesis that the formation of silver oxide is responsible for the increased fluorescence intensity. A somewhat large hysteresis is seen between the forward and reverse scans, which is likely due to the higher electric resistance of the Ag_2O film and its sluggish rate of electroreduction. The right panel of Figure 4a displays three fluorescence images of the Ag microelectrode collected at three potentials during the potential sweep.

We also studied the stability of the electrochemically formed silver oxide film on the Ag microelectrode by holding the electrode potential at +0.5 V vs Pt QRE for 7.33 s and then disconnecting the circuit and watching the time-dependent

fluorescence decay. As shown in Figure 4b, the fluorescence of the oxidized Ag surface decreased by nearly 90% within 3 s after disconnecting the circuit. This result suggests that the Ag_2O photodissociation and dissolution are rapid even for the large 100 μm microelectrode. Since the rate of diffusion is inversely related to the diameter of the electrode, one can expect that the diffusion-driven Ag_2O dissolution on a 40 nm Ag particle can be several orders of magnitude faster than that on the Ag disk microelectrode. Therefore, dissolution and photodissociation of Ag_2O can be responsible for the observed fast fluorescence decrease after Ag nanoparticle collision.

The use of the Pt nanocell and fluorescence microscopy has enabled us to capture some remarkable characteristics of the

collision and dissolution behavior of single Ag nanoparticles on an electrode surface, which are otherwise undiscoverable from simple electrochemical measurements. First, nanoparticles undergo fast and repeated collisions with the electrode. Second, a drastic change in the fluorescence intensity can be clearly observed during particle collision and oxidation. Although the experiment in Figure 3 provides direct microscopic evidence for the dynamic particle motion during single particle collision, we note that our results are significantly different from previous observations. The most striking difference is that nanoparticle collision is significantly slower in the Pt nanocell compared to previous recordings in an open solution on a gold ultramicroelectrode which often finishes within ~ 20 ms for a 60 nm diameter Ag nanoparticle.²⁴ As shown in the following section, some particle collision processes can last for more than 60 s. Furthermore, the seemingly random nanoparticle motion is somewhat confined to a finite distance from the electrode surface.

The use of an even smaller 100 nm diameter nanocell (E100) has enabled continuous fluorescence recordings of single particle collision responses for more than 60 s. Figure 5a displays a series of five fluorescence images collected in a 60 s video of a 40 nm Ag nanoparticle in an E100 Pt nanocell under a +0.5 V applied potential. The fluorescence intensity is distinctly stronger when the particle moves close to the Pt surface. Interestingly, the range of motion extends out to a remarkable ~ 6 μm distance away from the Pt electrode. To better understand how the fluorescence intensity and location of the nanoparticle change with time, in Figure 5b, we plotted both the particle–electrode distance and fluorescence intensity with time. Figure 5b shows an apparent negative correlation between the fluorescence intensity of the nanoparticle and its distance from the electrode. When the Ag nanoparticle is close to the Pt, the fluorescence intensity can increase more than 10 times compared to its intensity prior to collision (*hereafter defined as its baseline intensity*). This position–intensity relationship can also be presented using a scatter plot as shown in Figure 5c. Most of the high intensities are found when the particle is within a small distance (i.e., 400 nm) from the Pt electrode. Once the nanoparticle is more than ~ 500 nm away from the Pt, its intensity quickly drops nearly to its baseline intensity.

Similar results can be found in the recordings collected at higher voltages. Figure S3a,b and S3c,d are fluorescence images and position–intensity plots taken at +1.0 V and +1.5 V, respectively, using the same E100 Pt nanocell. Figures 5c–e are their corresponding scatter plots of fluorescence intensity. The range of collisional particle motion is restricted to about 5 μm at +1.0 V and 4 μm at +1.5 V, which are smaller than that at +0.5 V. The negative correlation between the fluorescence intensity and particle–electrode distance still exists. However, particle intensity decays with distance a bit slower at higher voltages than at +0.5 V. Very interestingly, when even higher potentials are applied, we can sometimes observe more than one nanoparticles colliding with the electrode in the same nanocell, as shown in Figure S3c,d. With higher supporting electrolyte concentration (2 mM sodium citrate and 20 mM NaNO_3), the silver NPs can still be detected but with a much faster motion speed (Figure S4).

In Figure 5f, we plotted the probability of finding the nanoparticle along the nanocell at three different voltages. In all three conditions (+0.5 V, +1.0 V, and +1.5 V), the position distribution plot can be fitted by two Gaussian peaks. The most

probable position of finding the nanoparticle is at a distance between 600 to 800 nm away from the electrode. Another probable position is at a distance of about 2 μm . The measured peak-to-peak separations are 1.2, 1.0, and 0.8 μm at +0.5, +1.0, and +1.5 V, respectively. The presence of two highly probable positions suggests that the nanoparticle likely undergoes a yo-yo type oscillating motion between two highly probable positions in the nanocell.

Figure 5g is a schematic illustration of our proposed mechanism for the observed long-time and repeated nanoparticle collision behavior in a Pt nanocell. A key aspect in this proposed mechanism is the consideration of several strong and changing electrostatic interactions a silver nanoparticle may experience inside the small volume of a Pt nanocell. A negatively charged, citrate-capped Ag nanoparticle initially experiences strong electrostatic repulsion from the negatively charged quartz walls. This is confirmed by the nearly zero probability of observing particles in the nanocell prior to the application of a significant positive potential on the Pt. The application of a positive potential provides a strong attractive force to the negatively charged Ag nanoparticle greatly increasing the chance of observing a particle in the nanocell. Upon nanoparticle collision and partial oxidation on the Pt electrode, the Ag nanoparticle acquires positive charges on its surface and is immediately repelled from the electrode. The change in its surface potential from negative to positive, however, also changes the particle-wall electrostatic interaction from repulsion to attraction. Therefore, the now partially oxidized Ag nanoparticle should also be attracted toward the opposite end of the tip, indicated by the blue arrow in the second panel of Figure 5g. As suggested in our previous work,²⁴ the partially oxidized particle loses its positive charges by further silver dissolution and adsorption of citrate ions on its surface which changes the particle–electrode force from repulsion to attraction. When sufficient negative charges are accumulated on the Ag surface, the nanoparticle should be pulled back to the electrode causing another particle collision and oxidation to happen. This process repeats many times until either the particle is fully oxidized in the nanocell or it may be lost to the bulk solution.

Figure 5g provides a satisfactory explanation to the observations on Ag nanoparticle collision and oxidation on an electrode. First, single nanoparticle collision is a highly dynamic and repeated process. Once a nanoparticle enters the Pt nanocell, it undergoes repeated collision and oxidation on the Pt leading to transient changes in its surface potential. Oxidation of Ag is expected to proceed at higher electrode potentials leading to higher fluorescence intensities in Figure 5c. Furthermore, the Ag_2O dissolution process may take a longer time (and a longer travel distance) to finish at higher potentials. (Figure 5d,e)

The extremely small structure of the Pt nanocell explains some of the distinct differences between this work and the previous observations. There are two key factors one should consider when comparing the many seconds long collision processes to the ~ 20 ms short collision events observed on an ultramicroelectrode in an open solution. The presence of the negatively charged quartz walls can provide the initial attraction force upon particle oxidation which balances the strong electrostatic repulsion force from the electrode. This minimizes the chance of losing the particle to the bulk solution. Second, as our electrochemical recordings have shown, particle oxidation may be rather insufficient in a Pt nanocell due to hindered mass

and ion transport and the use of relatively low concentrations of supporting electrolyte. As such, it is possible that only a small portion of the Ag nanoparticle is oxidized during each subcollision event. Our fluorescence recordings have shown that most nanoparticles disappear within a few seconds in a larger 300 nm nanocell while it can take more than 60 s to finish in a 100 nm nanocell. This result confirms that mass transport should be largely responsible for the extended particle collision process.

Electrochemical Recording of Nanoparticle Collision in a Pt Nanocell. In addition to the fluorescence imaging experiments described above, we performed direct electrochemical recording of nanoparticle collision events in Pt nanocells. Interestingly, we were not able to detect obvious particle collision events when the applied voltage is below +2.0 V. This is in agreement with the insufficient and sluggish Ag oxidation caused by hindered mass and ion transfer resistance in the nanocell. Figure 6 shows a typical 60-s current–time

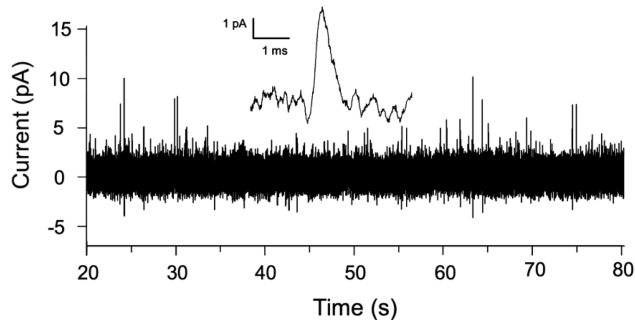


Figure 6. A representative 60-s current–time trace collected on an E100 nanocell at +2 V for the oxidation of 40 nm silver nanoparticles.

trace collected using an E100 nanocell filled with 40 nm Ag nanoparticles. One can see several sharp current spikes detected in this 60-s trace. Each current spike is only 5–10 pA high and has a triangular shape with a peak width less than 1 ms. This is in stark contrast to the current recordings collected on an ultramicroelectrode in a large solution volume where large current spikes of hundreds of pA are observed. The integrated charge under each spike can be used to calculate the amount of silver being oxidized during each collision subevent. The mean charge detected is about 2.7 fC at +2.0 V. This corresponds to only 1/4 monolayers (one monolayer of Ag atoms corresponds to 11 fC) of silver being oxidized on a 40 nm Ag nanoparticle.

CONCLUSIONS

In summary, we have developed a unique nanospectroelectrochemical method to image dynamic collision events of single silver nanoparticles at the electrode/solution interface. A key aspect of this method is the formation of a nanoscale electrode/solution interface inside a microfabricated nanocell. By depositing a Pt nanoelectrode at the tip of a quartz nanopipette, one can directly observe the dynamic collision and oxidation behavior of single Ag nanoparticles in a confined volume down to ~50 attoliters. There are two key factors leading to the successful imaging of dynamic collision behavior at the electrode/solution interface, (1) the somewhat balanced electrostatic interactions between the nanoparticle, the charged quartz wall, and the positively biased Pt electrode, and (2) the utilization of strong fluorescence emission of Ag nanoclusters formed from the oxidized Ag₂O product on the Ag nanoparticle

surface. The extremely small dimension of the nanocell reduces the background fluorescence signal and limits the nanoparticle motion to one dimension. Furthermore, the use of lower concentration of supporting electrolyte (e.g., 2 mM) allows the particle motion to be affected more effectively by both the quartz surface and the electrode over a larger distance. The development and use of a Pt nanocell may have significant impacts on studying particle and molecular dynamics at the electrode/solution interface for future studies, which cannot be easily obtained from ensemble measurements.

ASSOCIATED CONTENT

Supporting Information

The Supporting Information is available free of charge on the ACS Publications website at DOI: 10.1021/jacs.7b06431.

Excitation and emission spectra of 40 nm silver nanoparticles; more examples showing collision and motion of single silver nanoparticles inside Pt nanocells (PDF)

Video S1 showing nanoparticle motion in a Pt nanocell (AVI)

AUTHOR INFORMATION

Corresponding Author

*zhangb@uw.edu

ORCID

Bo Zhang: 0000-0002-1737-1241

Author Contributions

†R.H. and Y.F. contributed equally to this paper.

Notes

The authors declare no competing financial interest.

ACKNOWLEDGMENTS

We gratefully acknowledge financial support from AFOSR MURI (FA9550-14-1-0003) and the National Science Foundation (CHE-1515897). We also thank Professor Joshua Vaughan of University of Washington and Professor Henry White of University of Utah for helpful discussions. Part of this work was conducted at the Molecular Analysis Facility, a National Nanotechnology Coordinated Infrastructure site at the University of Washington which is supported in part by the National Science Foundation (grant ECC-1542101), the University of Washington, the Molecular Engineering & Sciences Institute, the Clean Energy Institute, and the National Institutes of Health.

REFERENCES

- (1) Oja, S. M.; Wood, M.; Zhang, B. *Anal. Chem.* **2013**, *85*, 473.
- (2) Anderson, T. J.; Zhang, B. *Acc. Chem. Res.* **2016**, *49*, 2625.
- (3) Fang, Y.; Wang, H.; Yu, H.; Liu, X.; Wang, W.; Chen, H.-Y.; Tao, N. J. *Acc. Chem. Res.* **2016**, *49*, 2614.
- (4) Wang, C.; Zhang, H. W.; Zhang, J. F.; Wu, D.; Tian, Z. Q.; Tian, Z. W.; Shi, K. *Electrochim. Acta* **2014**, *146*, 125.
- (5) Sambur, J. B.; Chen, P. *Annu. Rev. Phys. Chem.* **2014**, *65*, 395.
- (6) Shao, M.; Chang, Q.; Dodelet, J.-P.; Chenitz, R. *Chem. Rev.* **2016**, *116*, 3594.
- (7) Liu, H.; Nosheen, F.; Wang, X. *Chem. Soc. Rev.* **2015**, *44*, 3056.
- (8) Scofield, M. E.; Liu, H.; Wong, S. S. *Chem. Soc. Rev.* **2015**, *44*, 5836.
- (9) Nie, Y.; Li, L.; Wei, Z. *Chem. Soc. Rev.* **2015**, *44*, 2168.
- (10) Strasser, P. *Acc. Chem. Res.* **2016**, *49*, 2658.
- (11) Zeng, M.; Li, Y. J. *Mater. Chem. A* **2015**, *3*, 14942.

- (12) Morales-Guio, C. G.; Stern, L.-A.; Hu, X. *Chem. Soc. Rev.* **2014**, *43*, 6555.
- (13) Stratakis, E.; Kymakis, E. *Mater. Today* **2013**, *16*, 133.
- (14) Chen, F.-C.; Wu, J.-L.; Lee, C.-L.; Hong, Y.; Kuo, C.-H.; Huang, M. H. *Appl. Phys. Lett.* **2009**, *95*, 182.
- (15) Tian, Y.; Tatsuma, T. *Chem. Commun.* **2004**, 1810.
- (16) Pillai, S.; Green, M. A. *Sol. Energy Mater. Sol. Cells* **2010**, *94*, 1481.
- (17) Quinn, B. M.; van 't Hof, P.; Lemay, S. G. *J. Am. Chem. Soc.* **2004**, *126*, 8360.
- (18) Xiao, X.; Bard, A. J. *J. Am. Chem. Soc.* **2007**, *129*, 9610.
- (19) Xiao, X.; Fan, F.-R. F.; Zhou, J.; Bard, A. J. *J. Am. Chem. Soc.* **2008**, *130*, 16669.
- (20) Cheng, W.; Compton, R. G. *TrAC, Trends Anal. Chem.* **2014**, *58*, 79.
- (21) Zhou, Y.-G.; Rees, N. V.; Pillay, J.; Tshikhudo, R.; Vilakazi, S.; Compton, R. G. *Chem. Commun.* **2012**, 48, 224.
- (22) Zhou, Y.-G.; Rees, N. V.; Compton, R. G. *Angew. Chem., Int. Ed.* **2011**, *50*, 4219.
- (23) Ustarroz, J.; Kang, M.; Bullions, E.; Unwin, P. R. *Chem. Sci.* **2017**, *8*, 1841.
- (24) Oja, S. M.; Robinson, D. A.; Vitti, N. J.; Edwards, M. A.; Liu, Y.; White, H. S.; Zhang, B. *J. Am. Chem. Soc.* **2017**, *139*, 708.
- (25) Ma, W.; Ma, H.; Chen, J.-F.; Peng, Y.-Y.; Yang, Z.-Y.; Wang, H.-F.; Ying, Y.-L.; Tian, H.; Long, Y.-T. *Chem. Sci.* **2017**, *8*, 1854.
- (26) Fan, Y.; Han, C.; Zhang, B. *Analyst* **2016**, *141*, 5474.
- (27) Hao, R.; Fan, Y.; Zhang, B. *J. Electrochem. Soc.* **2016**, *163*, H3145.
- (28) Percival, S. J.; Zhang, B. *J. Phys. Chem. C* **2016**, *120*, 20536.
- (29) Dick, J. E.; Bard, A. J. *J. Am. Chem. Soc.* **2015**, *137*, 13752.
- (30) Hao, R.; Zhang, B. *Anal. Chem.* **2016**, *88*, 8728.
- (31) Kwon, S. J.; Fan, F.-R. F.; Bard, A. J. *J. Am. Chem. Soc.* **2010**, *132*, 13165.
- (32) Lebegue, E.; Anderson, C. M.; Dick, J. E.; Webb, L. J.; Bard, A. J. *Langmuir* **2015**, *31*, 11734.
- (33) Alligrant, T. M.; Dasari, R.; Stevenson, K. J.; Crooks, R. M. *Langmuir* **2015**, *31*, 11724.
- (34) Kim, J.; Kim, B.-K.; Cho, S. K.; Bard, A. J. *J. Am. Chem. Soc.* **2014**, *136*, 8173.
- (35) Jena, B. K.; Percival, S. J.; Zhang, B. *Anal. Chem.* **2010**, *82*, 6737.
- (36) Li, Y.; Cox, J. T.; Zhang, B. *J. Am. Chem. Soc.* **2010**, *132*, 3047.
- (37) Hao, R.; Zhang, B. *Anal. Chem.* **2016**, *88*, 614.
- (38) Zhou, M.; Yu, Y.; Hu, K.; Xin, H. L.; Mirkin, M. V. *Anal. Chem.* **2017**, *89*, 2880.
- (39) Dasari, R.; Tai, K.; Robinson, D. A.; Stevenson, K. J. *ACS Nano* **2014**, *8*, 4539.
- (40) Li, T.; He, X.; Zhang, K.; Wang, K.; Yu, P.; Mao, L. *Chem. Sci.* **2016**, *7*, 6365.
- (41) Sundaresan, V.; Marchuk, K.; Yu, Y.; Titus, E. J.; Wilson, A. J.; Armstrong, C. M.; Zhang, B.; Willets, K. A. *Anal. Chem.* **2017**, *89*, 922.
- (42) Fang, Y.; Wang, W.; Wo, X.; Luo, Y.; Yin, S.; Wang, Y.; Shan, X.; Tao, N. *J. Am. Chem. Soc.* **2014**, *136*, 12584.
- (43) Fosdick, S. E.; Anderson, M. J.; Nettleton, E. G.; Crooks, R. M. *J. Am. Chem. Soc.* **2013**, *135*, 5994.
- (44) Brasiliense, V.; Patel, A. N.; Martinez-Marrades, A.; Shi, J.; Chen, Y.; Combellas, C.; Tessier, G.; Kanoufi, F. *J. Am. Chem. Soc.* **2016**, *138*, 3478.
- (45) Batchelor-Mcauley, C.; Martinez-Marrades, A.; Tschulik, K.; Patel, A. N.; Combellas, C.; Kanoufi, F.; Tessier, G.; Compton, R. G. *Chem. Phys. Lett.* **2014**, *597*, 20.
- (46) Patel, A. N.; Martinez-Marrades, A.; Brasiliense, V.; Koshelev, D.; Besbes, M.; Kuszelewicz, R.; Combellas, C.; Tessier, G.; Kanoufi, F. *Nano Lett.* **2015**, *15*, 6454.
- (47) Brasiliense, V.; Berto, P.; Combellas, C.; Kuszelewicz, R.; Tessier, G.; Kanoufi, F. *Faraday Discuss.* **2016**, *193*, 339.
- (48) Ovesný, M.; Křížek, P.; Borkovec, J.; Švindrych, Z.; Hagen, G. M. *Bioinformatics* **2014**, *30*, 2389.
- (49) Guerrette, J. P.; Oja, S. M.; Zhang, B. *Anal. Chem.* **2012**, *84*, 1609.
- (50) Zoski, C. G.; Mirkin, M. V. *Anal. Chem.* **2002**, *74*, 1986.
- (51) Peyser, L. A.; Vinson, A. E.; Bartko, A. P.; Dickson, R. M. *Science* **2001**, *291*, 103.
- (52) Peyser, L. A.; Lee, T. H.; Dickson, R. M. *J. Phys. Chem. B* **2002**, *106*, 7725.